This article has been accepted for publication in a future issue of this journal, but has not been fully edited. Content may change prior to final publication.

TPEL-Reg-2012-10-1336   1

A High Step-Up Three-Port DC-DC Converter for Stand-Alone PV/Battery Power Systems

Yen-Mo Chen, *Student Member, IEEE*, Alex Q. Huang, *Fellow, IEEE*, and Xunwei Yu, *Student Member, IEEE*

Abstract—A three-port dc-dc converter integrating PV and battery power for high step-up applications is proposed in this paper. The topology includes five power switches, two coupled inductors and two active-clamp circuits. The coupled inductors are used to achieve high step-up voltage gain and to reduce the voltage stress of input side switches. Two sets of active-clamp circuits are used to recycle the energy stored in the leakage inductors and to improve the system efficiency. The operation mode does not need to be changed when a transition between charging and discharging occur. Moreover, tracking maximum power point of the PV source and regulating the output voltage can be operated simultaneously during charging/discharging transitions. As long as the sun irradiation level is not too low, the maximum power point tracking (MPPT) algorithm will be disabled only when the battery charging voltage is too high. Therefore, the control scheme of the proposed converter provides maximum utilization of PV power most of the time. As a result, the proposed converter has merits of high boosting level, reduced number of devices, and simple control strategy. Experimental results of a 200W laboratory prototype are presented to verify the performance of the proposed three-port converter.

Index Terms—*Three-port converter, high step-up application, DC microgrid, hybrid power system, renewable energy source, energy storage.*

I. INTRODUCTION

INTEGRATED multiport converters for interfacing several power sources and storage devices are widely used and discussed in recent years. Instead of using individual power electronic converters for each of the energy sources, multiport converters have the advantages including less components, lower cost, more compact size and better dynamic performance. In many cases, at least one energy storage device should be incorporated For example, in the electric vehicle application, the regenerative energy occurs during acceleration or startup. Therefore, it is very important for the port connected to the energy storage to allow bidirectional power flow.

Various kinds of topologies have been proposed due to the advantages of multiport converters. The combination strategies for the multiport converter include sharing switches, capacitors, inductors, or magnetic cores [1]. One could select a proper topology by considering many aspects such as cost, reliability, and flexibility depending on the applications. An application of hybrid energy supply using renewable energy sources and storage devices is shown in Fig. 1. The DC microgrid enabled by the solid state transformer (SST) in the Future Renewable Electric Energy Delivery and Management System (FREEDM System) integrates various distributed renewable energy resources (DRERs) and distributed energy storage devices (DESDs) [2]. For instance, if solar power is selected as the renewable energy source and battery as the storage device, the battery can either supply the load with the solar energy at the same time or store the excess power from the solar panels for backup use. Therefore, the bidirectional power path must be provided for the battery port. The dc-dc converters interfacing the DRERs or DESDs are expected to have relative high voltage conversion ratios since the dc bus of the FREEDM system is 380V. It is studied that for the dc-dc converters connected to the solar panels, voltage gain extension cells such as coupled inductors, transformers, and switched capacitors are often employed to achieve high voltage conversion ratios [3]. By utilizing the voltage gain extension cells, the extreme duty cycles that exist in typical boost converters can be avoided and the voltage stress on switches can be reduced. Thus, power switches with lower voltage rating and lower turn-on resistance can be chosen for the converters to reduce conduction losses. A converter using coupled inductors is relative better than isolation transformers since the coupled inductors have simpler winding structure and lower conduction loss [4]. However, the leakage inductors of the coupled inductors will consume significant energy for a large winding ratio. In such case, the voltage stress and the loss of the switches will both be increased. A boost converter with coupled inductor and active-clamp circuit is proposed in [4]. This boost converter can yield a high step-up voltage gain, reduce the voltage stress on switches, and recycle the energy in the leakage inductor.

Many multiport converter topologies have been presented in the literature and can be roughly divided into two categories. One is nonisolated type [5]-[13]: the nonisolated converters are

usually derived from the typical buck, boost or buck-boost topologies and are more compact in size. The other is isolated type [14]-[24]: the isolated converters using bridge topologies and multi-winding transformers to match wide input voltage ranges.

A topology based on buck configuration was used in spacecraft front-end system [5]-[6]. The battery port in this converter is unidirectional so the battery cannot be charged from the PV port. The modeling of this converter is discussed but the interacting control loops is not decoupled. A multi-input buck-boost type converter is proposed to interface many renewable energy sources [7] but there is no bidirectional port to interface the battery. A two-input converter for hybrid FC/battery power system is described in [8] with ZVS feature. Although the efficiency is improved, this converter could not provide a high voltage conversion ratio and bidirectional functionality. A multiple-input converter based on boost topology is presented in [9] have lower input current ripple and therefore is suitable for the large current applications such as hybrid vehicles. Another three-input boost converter interfaces two unidirectional input ports and one bidirectional port is presented in [10] for hybrid PV/FC/battery system. Two types of decoupling networks are introduced based on the utilization state of battery. A multi-input SEPIC with a bi-directional input is proposed in [11]. This converter is suitable for the hybrid system that incorporates energy storage elements such as ultra-capacitors. However, lack of voltage gain extension cells makes the converters in [9]-[11] difficult to be used in a high step-up application. Moreover, for the converters in [10]-[11], the operation mode has to be changed after a transition between charging and discharging occurs. This would increase the complexity of the control scheme and might reduce the reliability of the system.

A time-sharing multiple-input converter using active clamping technique is proposed in [14]. The converter provides two isolated ports, which is overqualified for our application. Bidirectional port in [11] can be added into this time-sharing converter to form an isolated three-port converter but the power stage and the control scheme will become complicated. Many isolated three-port converters with half-bridge [15]-[17] or full-bridge [18]-[21] topologies are suitable for high step-up applications since a multi-winding transformer is adopted. These isolated three-port converters could achieve galvanic isolation and bidirectional capabilities but the amount of active switches results in complicated driving circuits and large size. A converter based on the boost-dual-half bridge topology is presented in [15]. This converter is composed of three half-bridges and a three-winding transformer and is suitable for high step-up applications. However, the amount of active switches, input inductors and filter capacitors would increase the cost and size of the converter. Another three-port triple-half-bridge converter using a combined phase-shift and PWM control to manage the bidirectional power flow is presented in [16]. However, the same duty cycle is given to all three half-bridges and is the only variable regulating the voltage level. Therefore, this converter can only be used in the applications where single power source or storage element is

connected unless additional voltage control loop that allows different duty cycles is introduced. A converter utilizing flux additivity in a multi-winding transformer is presented in [18]. Although this topology can simultaneously transfer power from different ports, the reverse-blocking diodes only allow unidirectional power flow therefore the converter is not suitable for in the applications requires energy storage elements. In [21], a three-port bidirectional converter with three active-full-bridges, a three-winding transformer and two series-resonant tanks is reported. The transformer provides full isolation among all ports and wide input voltage range. The switching losses are reduced due to soft switching operation. The full-bridge topology is good for relative high power application but requires more power switches and complicated circuit design. Integrated three-port converters derived from half bridge converter are presented in [22]-[24] to interface PV and battery power. Small-signal modeling and decoupling network is introduced in [23] to design the compensators separately for the cross-coupled control loops. A family of three-port half-bridge converters is described in [24] and the primary circuit can function as a synchronous rectification buck converter. Therefore, the converters in [22]-[24] are suitable for stand-alone step-down applications. Many other multi-input topologies are discussed in [13] and [25].

In this paper, a high step-up three-port dc-dc converter for the hybrid PV/battery system is proposed with the following advantages: 1) high voltage conversion ratio is achieved by using coupled inductors; 2) simple converter topology which has reduced number of the switches and associate circuits; 3) simple control strategy which does not need to change the operation mode after a charging/discharging transition occur unless the charging voltage is too high; 4) Output voltage is always regulated at 380V under all operation modes. It is noted that for the MPP-tracking converters, operating range has to be limited to the voltage less than the MPP voltage when the output voltage or current control is active [26]. This issue could be addressed by limiting the operating range of the converter in the voltages higher than MPP.

As shown in Fig.1, comparing to the typical multi-converter configuration that requires individual microcontroller for each converter, the integrated three-port converters is controlled by a single microcontroller. The communication interface utilized in the multi-converter configuration could be removed due to centralized control of the proposed converter. Therefore, the system cost and volume can be reduced. The major contribution of this paper is to propose an integrated three-port converter as a nonisolated alternative other than typical isolated topologies for high step-up three-port applications. The proposed switching strategy allows the converter to be controlled by the same two duty cycles in different operation modes. The detailed analysis is given in the following sections: The principle of operation is described in Section II. The PV source modeling, topological modes and ZVS conditions are analyzed in Section III. The modeling and control strategy is explained in Section IV. Finally, the experimental results are presented in Section V.
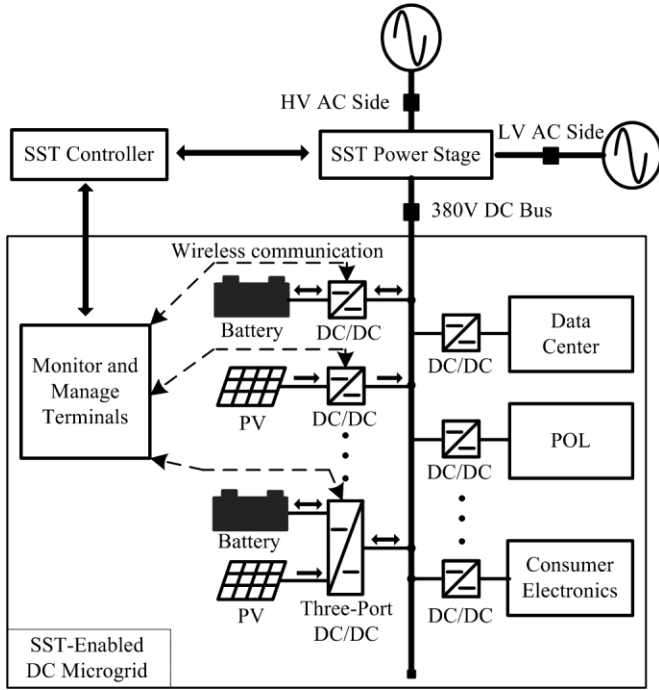
Fig. 1. Part of FREEDM system diagram showing SST-enabled DC

II. PRINCIPLE OF OPERATION

This section introduces the topology of proposed nonisolated three-port dc-dc converter, as illustrated in Fig. 2. The converter is composed of two main switches S_1 and S_2 for the battery and PV port. Synchronous switch S_3 is driven complementarily to S_1 such that bidirectional power flow for the battery port can be achieved. Two coupled inductors with winding ratios n_1 and n_2 are used as voltage gain extension cells. Two sets of active-clamp circuits formed by S_4, L_{k1}, C_{C1} and $S_5, L_{k2,} C_{C2}$ are used to recycle the leakage energy. L_{k1} and L_{k2} are both composed of a small leakage inductor from the coupled inductor and an external leakage inductor. Two independent control variables, duty cycles d_1 and d_2, allow the control over two ports of the converter while the third port is for the power balance. The fixed-frequency driving signals of the auxiliary switches S_3 and S_4 are complementary to primary switch S_1. Again, S_3 provides a bidirectional path for the battery port. Similarly, S_5 is driven in a complementary manner to S_2. A 180-degree phase-shift is applied between the driving signals of S_1 and S_2.

There are four operation periods based on the available solar power. First, the sun is in the eclipse stage and the solar irradiation is either unavailable or very low. This operation period is defined as period 1, and the battery will serve as the main power source. As the sun starts to shine and the initial solar irradiation is enough for supplying part of the load demand, the operation period is changed to period 2. The load is supplied by both solar and battery power in this period. For period 3, the increasing insolation makes the solar power larger than the load demand. The battery will preserve extra solar power for backup use. During period 4, the charging voltage of the battery reaches the preset level and should be limited to
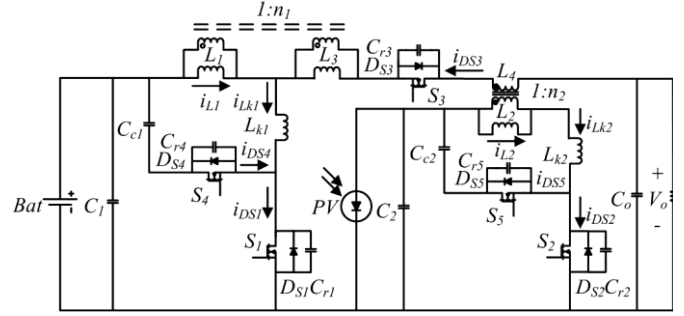

Fig. 2. Topology of the proposed converter.

prevent overcharging.

According to the solar irradiation and the load demand, the proposed three-port converter can be operated under two modes. In the battery balance mode (mode 1), MPPT is always operated for the PV port to draw maximum power from the solar panels. Battery port will maintain the power balance by storing the unconsumed solar power during light load condition or providing the power deficit during heavy load condition. The power sharing of the inputs can be represented as:

$$P_{load} = P_{pv\_SVC} + P_{bat\_SVC} \tag{1}$$

where P_{load} is the load demand power, P_{pv_SVC} is the PV power under solar voltage control (SVC) and P_{bat_SVC} is the battery power under SVC. In mode 1, maximum power is drawn from the PV source. Battery may provide or absorb power depending on the load demand. Therefore, P_{bat_SVC} could be either positive or negative. When the battery charging voltage is higher than the maximum setting, the converter will be switched into battery management mode (mode 2). In mode 2, MPPT will be disabled therefore only part of the solar power is drawn. However, the battery voltage could be controlled to protect the battery from overcharging. The power sharing of the inputs can be represented as:

$$P_{load} = P_{pv\_BVC} + P_{bat\_BVC} \tag{2}$$

where P_{pv_BVC} is the PV power under battery voltage control (BVC) and P_{bat_BVC} is the battery charging power under SVC. If the load is increased and the battery voltage is reduced, the converter will be switched to mode 1. The output voltage is always kept at 380V in both modes.

III. TOPOLOGICAL MODES AND ANALYSIS

A. PV Source Modeling

It is well explained in the literature [29-32] that using a PV generator as input source has significant effect on the converter dynamics. The non-linear V-I characteristic of a PV generator can be modeled using current source, diode, and resistors. The single-diode model shown in Fig. 3(a) is widely used for the PV source modeling. This model provides a trade-off between accuracy and complexity [33]. Thevenin's equivalent model with non-constant voltages and resistances has been proposed
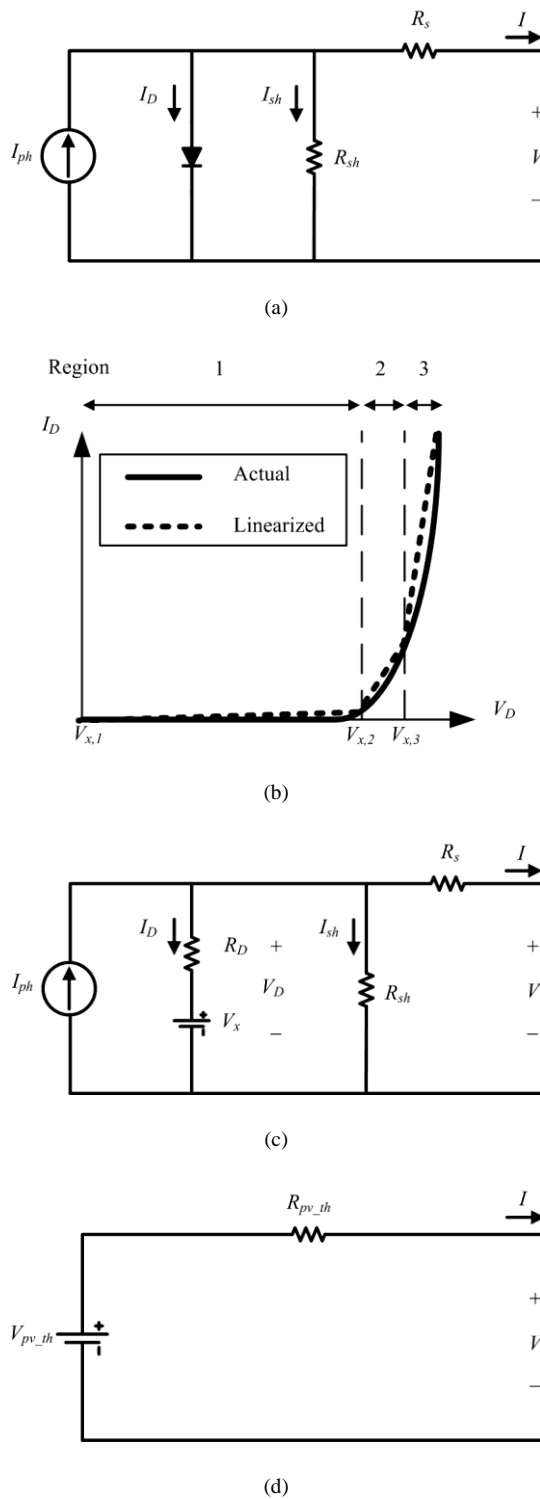
(a)

(b)

(c)

(d)

Fig. 3. Thevenin's equivalent circuit derived from the single-diode model. (a) Single-diode model of a PV generator.(b) V-I characteristic of diode: actual and linear approximation [34]. (c) Single-diode model with linearized diode. (d) Thevenin's equivalent circuit for single-diode model with linearized diode.

in [35-38] to closely approximate the characteristic of PV generator. The Thevenin-based model provides simpler prediction and computation for the maximum power point of PV array under different operating conditions.

Thevenin's theorem is not valid for a non-linear model, but

the non-linear model could be represented by a linear one with non-constant parameters [36]. In [37], for example, the piecewise linearization is used to linearize the diode. The parameters in Fig. 3(a) can be estimated using the manufacturer's datasheet [39]. As shown in Fig. 3(b), the actual diode characteristic has been divided into three regions and the characteristic in each region is approximated as a straight line. Each line can be further represented by a set of voltage source $V_{x,n}$ and resistance $R_{D,n}$ (n=1,2,3). The approximation of piecewise linearization would be more accurate as the number of regions increased. At the boundary points of regions, the values of linearized characteristic are exactly the same as actual characteristic. Therefore, the maximum power point of the PV generator is chosen as one of the boundary points such that the operation at this point has no approximation error. The single-diode model of the PV generator with linearized diode is shown in Fig. 3(c), where the diode is approximated by the voltage source V_x, and resistance R_D. The values of V_x and R_D are dependent to the operation region of the PV generator. The Thevenin's equivalent model of Fig. 3(c) is shown in Fig. 3(d). From the derivation in [35], the $V_{pv\_th,n}$ and $R_{pv\_th,n}$ can be calculated by:

$$V_{pv\_th,n} = V_{x,n} + R_{D,n} \cdot \frac{R_{sh} \cdot I_{ph} - V_{x,n}}{R_{sh} + R_{D,n}} \qquad (3)$$

$$R_{pv\_th,n} = R_s + \frac{R_{sh} \cdot R_{D,n}}{R_{sh} + R_{D,n}} \qquad (4)$$

For the following discussion, Thevenin's equivalent model is adopted for the PV generator modeling.
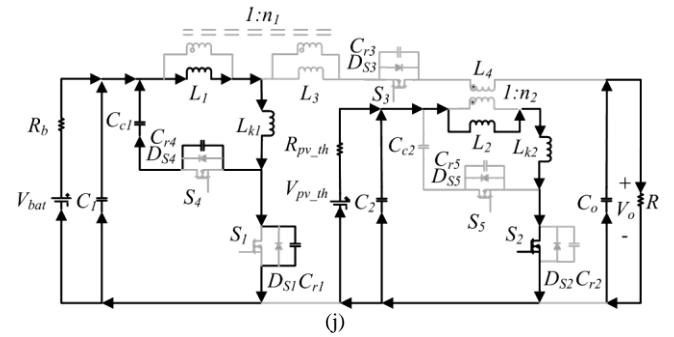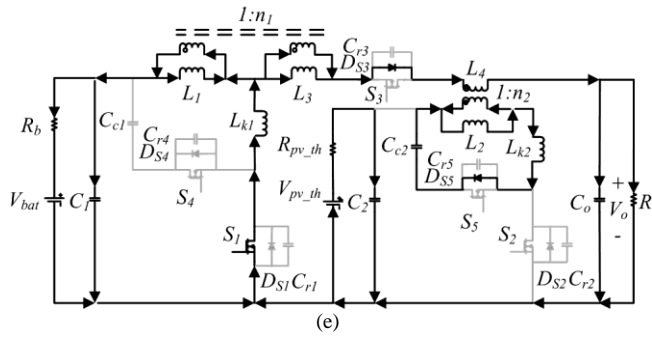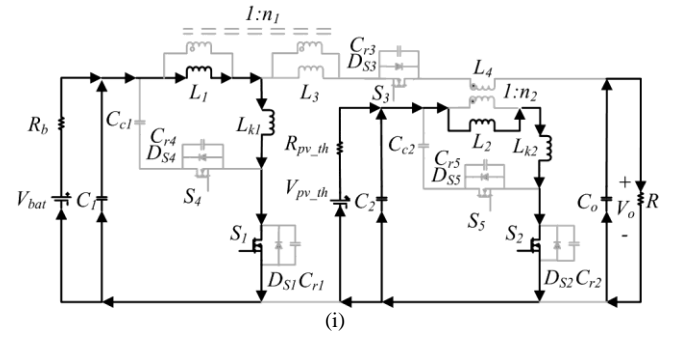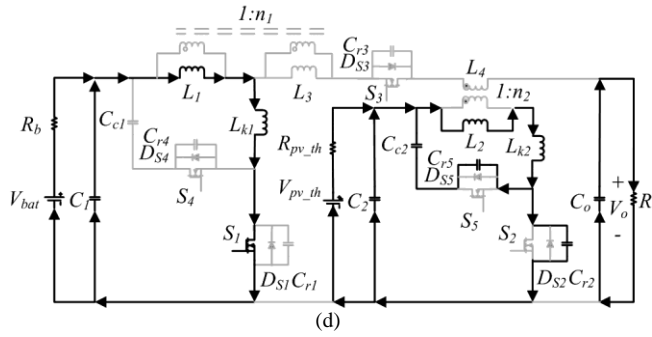
B. Operation of the topological modes

Before performing the analysis, some assumptions should be made: i)The switches are assumed to be ideal; ii)The magnetizing inductors are large enough so that the current flows through the inductors are constant; iii)The capacitors are large enough so that the voltages across the capacitors are constant. The topological modes over a switching cycle are shown in Fig. 4 and key waveforms of the proposed converter are given in Fig. 5. Detailed explanation of each interval is given as follows:

Interval 1 [Fig. 4(a), $t_0 \leq t < t_1$]: At t_0, S_1 and auxiliary switches S_4 and S_5 are turned off while primary switch S_2 is turned on. Although S_1 is in the off-state, resonant inductor L_{k1} resonates 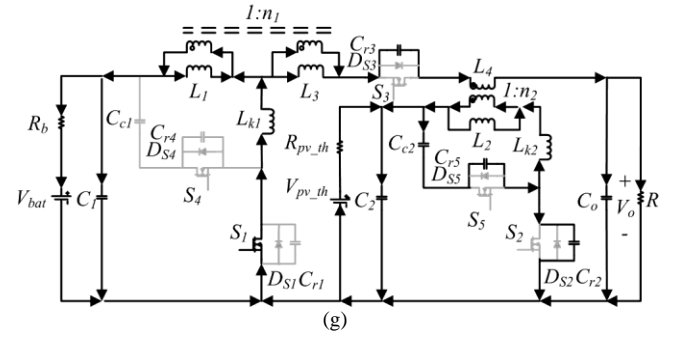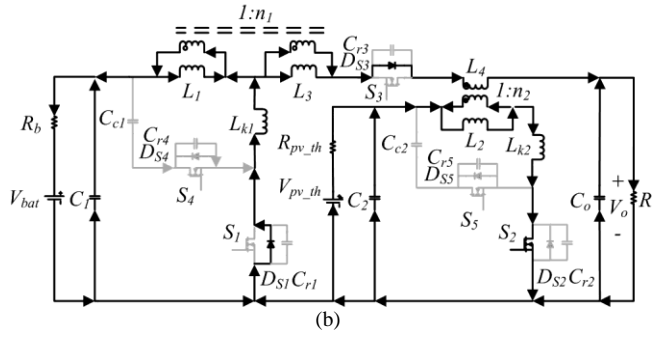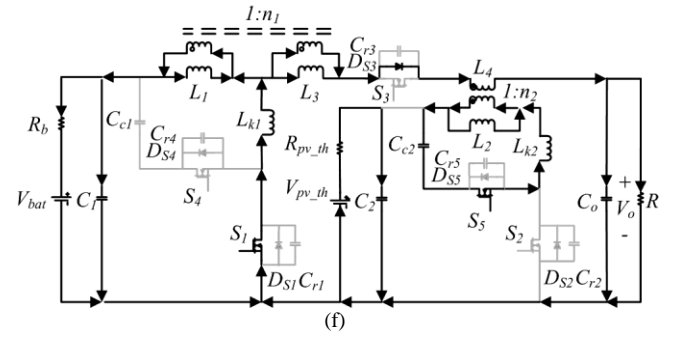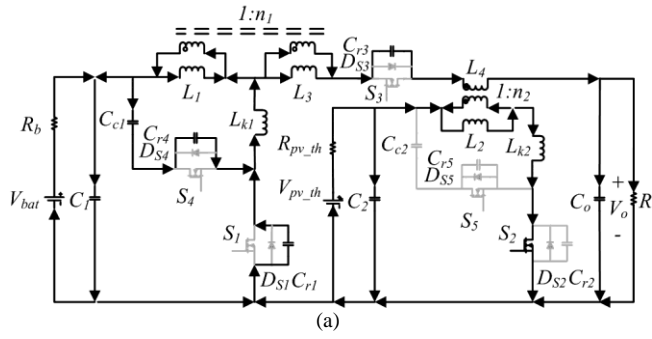with C_{r1} and C_{r4}. In this period, C_{r1} is discharged to zero and C_{r4} is charged to $V_{bat}+V_{Cc1}$. For the PV port, S_2 is turned on and the current from the PV panels flow through V_{pv_th}-L_2-L_{k2}-S_2 loop. In order to achieve the ZVS feature for S_1, the energy stored in resonant inductor L_{k1} should satisfy the following inequality:

$$0.5 \times L_{k1} \times \left[i_{Lk1}(t_0)\right]^2 \geq 0.5 \times (C_{r1} \| C_{r4}) \times \left[v_{DS1}(t_0)\right]^2 \qquad (5)$$

Interval 2 [Fig. 4(b), $t_1 \leq t < t_2$]: This mode starts when v_{ds1} is down to zero. The body diode of S_1 is forward biased so that the ZVS condition for S_1 is established. The resonant current i_{Lk1} is increased toward zero. L_2 is still linearly charged in this period.

This article has been accepted for publication in a future issue of this journal, but has not been fully edited. Content may change prior to final publication.

TPEL-Reg-2012-10-1336 5

(a)

(f)

(b)

(g)

(c)

(h)

(d)

(i)

(e)

(j)

This article has been accepted for publication in a future issue of this journal, but has not been fully edited. Content may change prior to final publication.

TPEL-Reg-2012-10-1336   6
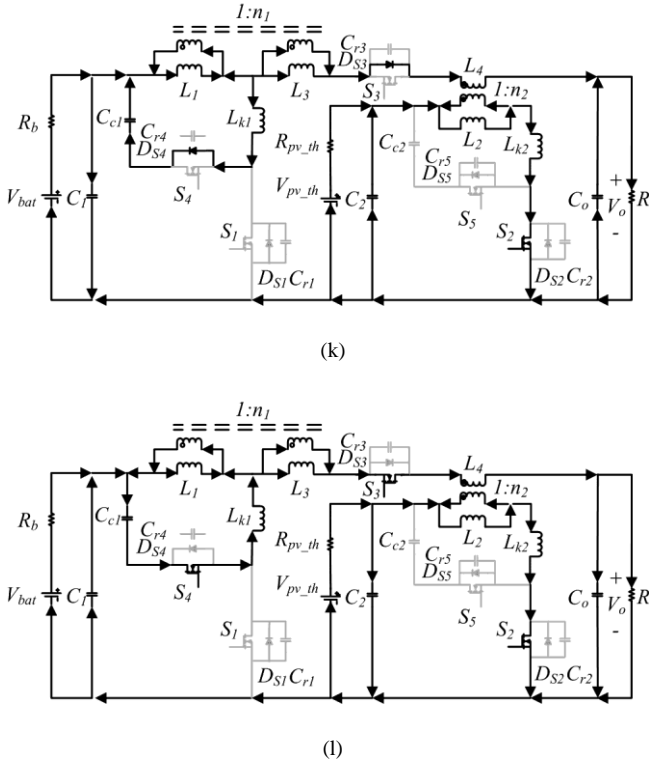
(k)

(l)

Fig. 4. Topological modes of the proposed converter. (a) Interval 1. (b) Interval 2. (c) Interval 3. (d) Interval 4. (e) Interval 5. (f) Interval 6. (g) Interval 7. (h) Interval 8. (i) Interval 9. (j) Interval 10. (k) Interval 11. (l) Interval 12.

Interval 3 [Fig. 4(c), $t_2 \leq t < t_3$]: S_1 begins to conduct current at t_2 and the battery port current follows the path V_{bat}-L_1-L_{k1}-S_1. S_2 is also turned on in this interval. Therefore, both L_1 and L_2 are linearly charged and energy of both input ports is stored in these magnetizing inductors. Auxiliary switches S_3, S_4, and S_5 are all turned off.

Interval 4 [Fig. 4(d), $t_3 \leq t < t_4$]: In this interval, S_2 starts to be turned off and the auxiliary switch S_5 remains in the off-state. However, a resonant circuit formed by L_{k2}, C_{r2}, and C_{r5} releases the energy stored in L_{k2}. Resonant capacitor C_{r2} is quickly charged to $V_{pv\_th}+V_{Cc2}$ while C_{r5} is discharged to zero. In order to achieve the $\overline{ZVS}$ feature for S_5, the energy stored in resonant inductor L_{k2} should satisfy the following inequality:

$$0.5 \times L_{k2} \times \left[i_{Lk2}(t_3) \right]^2 \geq 0.5 \times (C_{r2} \parallel C_{r5}) \times \left[v_{DS5}(t_3) \right]^2 \qquad (6)$$

Interval 5 [Fig. 4(e), $t_4 \leq t < t_5$]: At t_4, v_{ds5} reaches zero and the body diode across the auxiliary switch S_5 is turned on. Therefore, a ZVS condition for S_5 is established. Given that the C_{r5} is much smaller than C_{C2}, almost all the magnetizing current is recycled to charge the clamp capacitor C_{C2}. Furthermore, V_{Cc2} is considered as a constant value since the capacitance of C_{C2} is large enough. This interval ends when inductor current i_{Lk2} drops to zero.

Interval 6 [Fig. 4(f), $t_5 \leq t < t_6$]: At t_5, the current of L_{k2} is reversed in direction and energy stored in t_5 is released through the C_{C2}-S_5-L_{k2}-L_3 loop. This interval ends when S_5 is turned off.
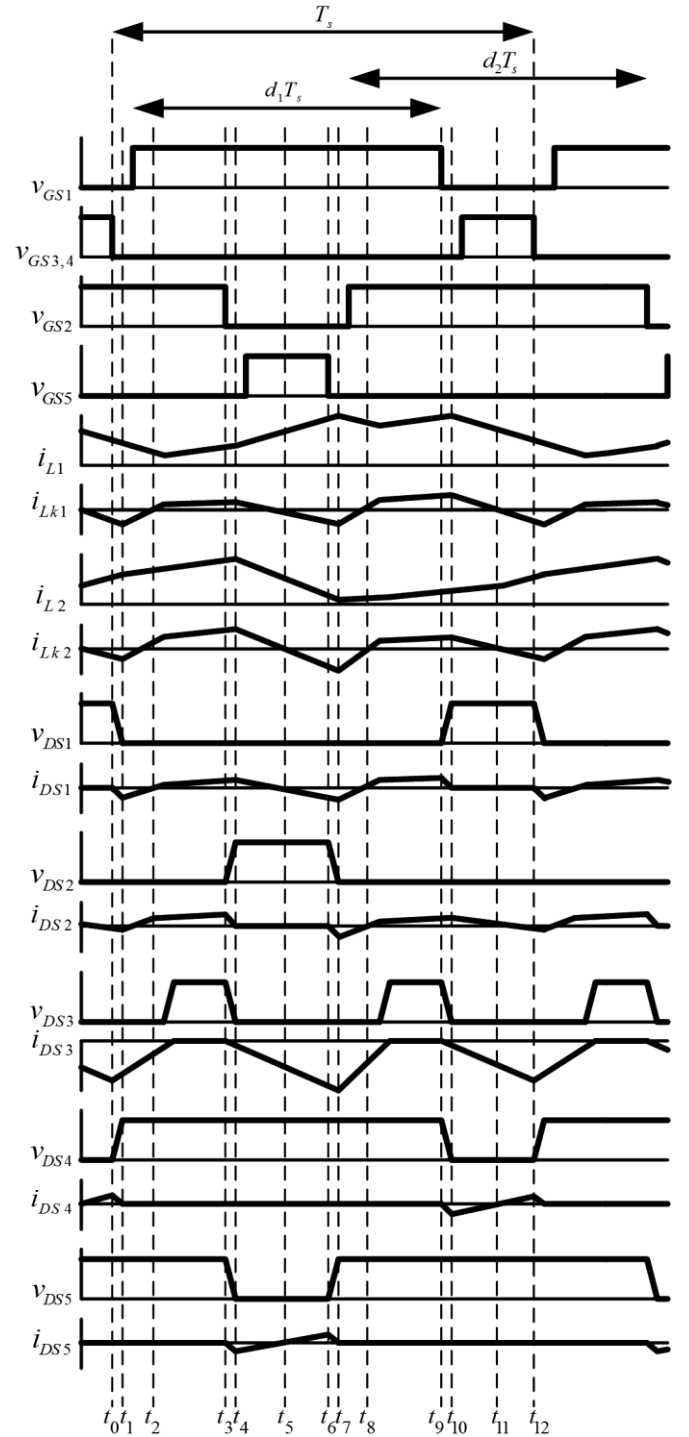
Fig. 5. Key waveforms of the proposed converter.

Interval 7 [Fig. 4(g), $t_6 \leq t < t_7$]: Switches S_2 and S_5 are both in the off-state at t_6. A resonant circuit is formed by L_{k2}, C_{r2}, and C_{r5}. During this interval, C_{r2} is discharged to zero and C_{r5} is charged to $V_{pv\_th}+V_{Cc2}$. To ensure the ZVS switching of S_2, the energy stored in L_{k2} should be greater than the energy stored in parasitic capacitors C_{r2} and C_{r5}:

$$0.5 \times L_{k2} \times \left[i_{Lk2}(t_6) \right]^2 \geq 0.5 \times (C_{r2} \parallel C_{r5}) \times \left[v_{DS2}(t_6) \right]^2 \qquad (7)$$

Interval 8 [Fig. 4(h), $t_7 \leq t < t_8$]: This interval starts when the voltage across C_{r2} is zero and the body diode D_{S2} is turned on. Leakage inductor current i_{Lk2} is linearly increased and the secondary side current of the coupled inductor is increased as well. The main switch S_2 should be turned on before i_{Lk2} becomes positive to ensure ZVS operation.

Interval 9 [Fig. 4(i), $t_8 \leq t < t_9$]: The circuit operation of interval 9 is identical to interval 3 since S_1 and S_2 are turned on in both intervals.

Interval 10 [Fig. 4(j), $t_9 \leq t < t_{10}$]: At t_9, S_1 is turned off while S_3 and S_4 remain in off-state. During this interval, L_{k1} will resonant with C_{r1} and C_{r4} to release the energy trapped in it. Resonant capacitor C_{r1} is charged to $V_{bat}+V_{Cc1}$ while C_{r4} is discharged to zero. To achieve the ZVS feature for S_4, the energy stored in resonant inductor L_{k2} should satisfy the following inequality:

$$0.5 \times L_{k1} \times \left[i_{Lk1}(t_9) \right]^2 \geq 0.5 \times (C_{r1} \| C_{r4}) \times \left[v_{DS4}(t_9) \right]^2 \quad (8)$$

Interval 11 [Fig. 4(k), $t_{10} \leq t < t_{11}$]: This interval begins when v_{ds4} drops to zero and the body diode across S_4 is turned on. The ZVS condition for S_4 is then established. Almost all the magnetizing current is recycled to charge C_{C1} since C_{r4} is much smaller than C_{C1}. Moreover, V_{Cc1} is considered as a constant value since the capacitance of C_{C1} is large enough. This interval ends when inductor current i_{Lk1} reaches zero.

Interval 12 [Fig. 4(l), $t_{11} \leq t < t_{12}$]:
The current flow through L_{k1} is reversed in direction at t_{11}, and the energy stored in C_{C1} is released through the C_{C1}-S_4-L_{k1}-L_1 loop. This interval ends when S_4 is turned off and the operation of the proposed converter over a switching cycle is complete.

C. ZVS Analysis

According to the (5)-(8), ZVS at turn-on transition could be achieved when enough energy is stored in the leakage inductors L_{k1} and L_{k2}. The ZVS conditions for switches S_1- S_4 should be determined by (5) and (7) since the ZVS transient periods of S_1 and v are less than that of S_4 and S_5. The voltages across switches S_1 and S_2 can be expressed as:

$$v_{DS1} = V_{bat} + V_{Cc1} = \frac{V_{bat}}{1-d_1} \quad (9)$$

$$v_{DS2} = V_{pv\_th} + V_{Cc2} = \frac{V_{pv\_th}}{1-d_2} \quad (10)$$

The peak current flow through S_1 and S_2 can be obtained as:

$$i_{DS1,peak} = i_{DS1} + \Delta i_1 = \frac{\frac{P_o}{\eta} - P_{pv\_th}}{V_{bat}d_1} + \frac{V_{bat}d_1 T_s}{2L_1} \quad (11)$$

$$i_{DS2,peak} = i_{DS2} + \Delta i_2 = \frac{\frac{P_o}{\eta} - P_{bat}}{V_{pv\_th}d_2} + \frac{V_{pv\_th}d_2 T_s}{2L_2} \quad (12)$$

where η represents the converter efficiency. It is noted that as long as $L_1 \gg L_{k1}$ and $L_2 \gg L_{k2}$, the behavior of converter duty cycle is approximately the same as for the non-active clamp converter in CCM. Typically, $L_{k1}= L_1/10$ and $L_{k2}= L_2/10$ can be

the conservative design guidelines. The effective duty cycles d_{eff1} and d_{eff2} are assumed to be equal to d_1 and d_2 for subsequent equations. As a result, the following inequalities can be derived from (9)-(12) to determine a proper leakage inductor:

$$L_{k1} \geq \frac{v_{DS1}^2 \left(C_{r1} \| C_{r4}\right)}{i_{DS1,peak}^2} = \frac{\left(\frac{V_{bat}}{1-d_1}\right)^2 \left(C_{r1} \| C_{r4}\right)}{\left(\frac{\frac{P_o}{\eta} - P_{pv\_th}}{V_{bat}d_1} + \frac{V_{bat}d_1 T_s}{2L_1}\right)^2} \quad (13)$$

$$L_{k2} \geq \frac{v_{DS2}^2 \left(C_{r2} \| C_{r5}\right)}{i_{DS2,peak}^2} = \frac{\left(\frac{V_{pv\_th}}{1-d_2}\right)^2 \left(C_{r2} \| C_{r5}\right)}{\left(\frac{\frac{P_o}{\eta} - P_{bat}}{V_{pv\_th}d_2} + \frac{V_{pv\_th}d_2 T_s}{2L_2}\right)^2} \quad (14)$$

IV. MODELING AND CONTROL STRATEGY

As mentioned in section II, the operation modes of the converter are determined by the conditions of available solar power and battery charging states. Controlling the converter in each mode requires different state variables to regulate voltages of the input and output ports. There are three control loops for the proposed converter: output voltage control (OVC), solar voltage control (SVC), and battery voltage control (BVC). The control scheme is shown in Fig. 6. The OVC is a simple voltage regulation loop. The SVC and BVC loops share the same control variable d_2 to achieve smooth mode transitions. SVC is used to regulate the voltage of the PV port and implement MPPT algorithm. BVC is the battery voltage regulation loop to prevent overcharging. It is noted that the PV port is operated under SVC most of the time. Therefore, BVC would not be active under normal operation. Only one control loop between SVC and BVC is performed. Moreover, once BVC starts to take control over d_2, SVC will be disabled immediately to avoid the noise issue caused by the MPPT algorithm [27]. In fact, the cross-coupled control loops is the intrinsic feature of the multiport converters since it is a high-order system. It will be a challenge to design the controllers of a multiport converter. Decoupling network for extracting separate transfer functions in such a system has been introduced by describing the system dynamics in a matrix form [23].

Small-signal modeling method is widely used for the power electronics converter. For a three-port converter which has two input ports, a matrix-form model will be very helpful to implement the closed-loop control and analyze the system dynamics. Since there are two operation modes for the proposed three-port converter, two sets of small-signal models will be derived. The state variables for each model are slightly different but the control variables are the same. The decoupling network is required for both models to allow separate controller design.
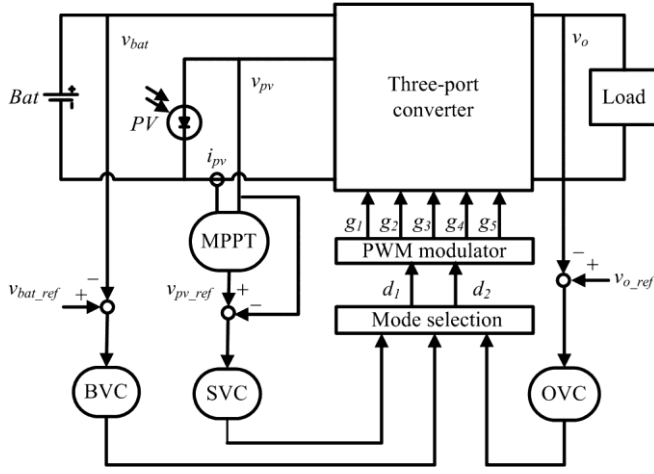
This article has been accepted for publication in a future issue of this journal, but has not been fully edited. Content may change prior to final publication.

TPEL-Reg-2012-10-1336   8

Fig. 6. Control scheme of the proposed three-port converter.

Fig. 7. Steady-state waveforms of the three-port converter.

A. Small-Signal Modeling in Battery Balance Mode

Four state variables including magnetizing inductor currents i_{L1} and i_{L2}, PV port voltage v_{C2}, output voltage v_o are selected to derive the small-signal model in this mode. From Fig. 7, a switching cycle can be divided into four main circuit stages depending on the on-off state of the two main switches. A set of state equations can be developed for each stage based on KCL and KVL.

Switching state 1 $[0 \le t < (d_1-(1-d_2))T_s/2]$: At $t=0$, primary switches S_1 and S_2 are turned on and auxiliary switches S_3, S_4, and S_5 are turned off. Inductors L_1 and L_2 are both charged and the power from the input ports is stored in the magnetizing inductors. The state equations can be represented in (15).

$$\begin{cases} L_1 \dfrac{di_{L1}}{dt} = v_{C1} \\[2mm] L_2 \dfrac{di_{L2}}{dt} = v_{C2} \\[2mm] C_2 \dfrac{dv_{C2}}{dt} = i_{L2} - \dfrac{\left(v_{pv\_th} - v_{C2}\right)}{R_{pv\_th}} \\[2mm] C_o \dfrac{dv_{Co}}{dt} = -\dfrac{v_o}{R} \end{cases} \tag{15}$$

Switching state 2 $[(d_1-(1-d_2))T_s/2 \le t < (d_1+(1-d_2))T_s/2]$: At $t=(d_1-(1-d_2))T_s/2$, switches S_1 and S_5 are turned on and switches S_2, S_3, and S_4 are turned off. Therefore, inductor L_1 is still charged but inductor L_2 is discharged.

$$\begin{cases} L_1 \dfrac{di_{L1}}{dt} = v_{C1} \\[2mm] L_2 \dfrac{di_{L2}}{dt} = \dfrac{-n_1 v_{C1} - v_o}{n_2} \\[2mm] C_2 \dfrac{dv_{C2}}{dt} = -\dfrac{\left(v_{pv\_th} - v_{C2}\right)}{R_{pv\_th}} \\[2mm] C_o \dfrac{dv_{Co}}{dt} = \dfrac{i_{L2}}{n_2} - \dfrac{v_o}{R} \end{cases} \tag{16}$$
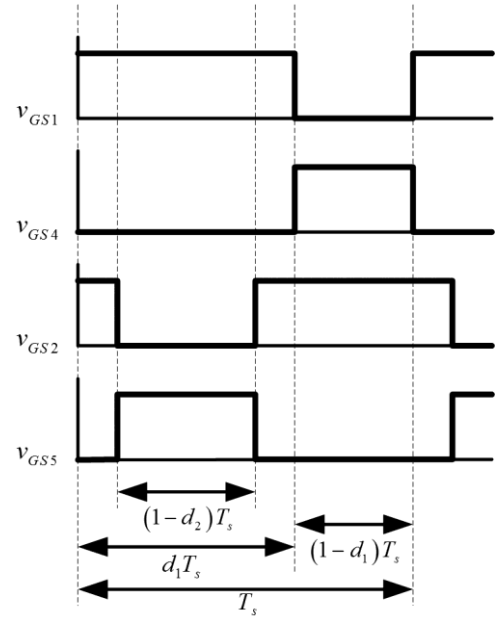
Switching state 3 $[(d_1+(1-d_2))T_s/2 \le t < d_1T_s]$: At $t=(d_1+(1-d_2))T_s/2$, switches S_1 and S_2 are turned on and switches S_3, S_4, and S_5 are turned off. Thus, inductors L_1 and L_2 are both charged again as in switching state 1.

$$\begin{cases} L_1 \dfrac{di_{L1}}{dt} = v_{C1} \\[2mm] L_2 \dfrac{di_{L2}}{dt} = v_{C2} \\[2mm] C_2 \dfrac{dv_{C2}}{dt} = i_{L2} - \dfrac{\left(v_{pv\_th} - v_{C2}\right)}{R_{pv\_th}} \\[2mm] C_o \dfrac{dv_{Co}}{dt} = -\dfrac{v_o}{R} \end{cases} \tag{17}$$

Switching state 4 $[d_1T_s \le t < T_s]$: At $t=d_1T_s$, switches S_2, S_3, and S_4 are turned on and switches S_1 and S_5 are turned off. Inductors L_1 is discharged but inductor L_2 is charged.

$$\begin{cases} L_1 \dfrac{di_{L1}}{dt} = \dfrac{\dfrac{v_{C1}}{(1-d_1)} - n_2 v_{C2} - v_o}{n_1} \\[3mm] L_2 \dfrac{di_{L2}}{dt} = v_{C2} \\[2mm] C_2 \dfrac{dv_{C2}}{dt} = \dfrac{n_2}{n_1} i_{L1} + i_{L2} - \dfrac{\left(v_{pv\_th} - v_{C2}\right)}{R_{pv\_th}} \\[2mm] C_o \dfrac{dv_{Co}}{dt} = \dfrac{i_{L1}}{n_1} - \dfrac{v_o}{R} \end{cases} \tag{18}$$

Using the volt-second balance and current-second balance theory [28], the state-space averaged equations can be obtained using (15)-(18):

This article has been accepted for publication in a future issue of this journal, but has not been fully edited. Content may change prior to final publication.

TPEL-Reg-2012-10-1336   9

$$L_1 : d_1 T_s v_{C1} + (1-d_1) T_s \frac{\frac{v_{C1}}{(1-d_1)} - n_2 v_{C2} - v_o}{n_1} = 0 \quad (19)$$

$$\rightarrow v_o = \frac{1+n_1 d_1}{1-d_1} v_{C1} - n_2 v_{C2}$$

$$L_2 : d_2 T_s v_{C2} + (1-d_2) T_s \frac{-n_1 v_{C1} - v_o}{n_2} = 0 \quad (20)$$

$$\rightarrow v_o = -n_1 v_{C1} + n_2 \frac{d_2}{1-d_2} v_{C2}$$

$$C_2 : (1-d_1) T_s \frac{n_2}{n_1} i_{L1} + d_2 T_s i_{L2} = T_s \frac{(v_{pv\_th} - v_{C2})}{R_{pv\_th}} \quad (21)$$

$$C_o : (1-d_1) T_s \frac{i_{L1}}{n_1} + (1-d_2) T_s \frac{i_{L2}}{n_2} = T_s \frac{v_o}{R} \quad (22)$$

From (17)-(20), the state-space averaged model is shown as:

$$\begin{cases} L_1 \frac{di_{L1}}{dt} = d_1 v_{C1} + (1-d_1) \frac{\frac{v_{C1}}{(1-d_1)} - n_2 v_{C2} - v_o}{n_1} \\ L_2 \frac{di_{L2}}{dt} = d_2 v_{C2} + (1-d_2) \frac{-n_1 v_{C1} - v_o}{n_2} \\ C_2 \frac{dv_{C2}}{dt} = (1-d_1) \frac{n_2}{n_1} i_{L1} + d_2 i_{L2} - \frac{(v_{pv\_th} - v_{C2})}{R_{pv\_th}} \\ C_o \frac{dv_o}{dt} = (1-d_1) \frac{i_{L1}}{n_1} + (1-d_2) \frac{i_{L2}}{n_2} - \frac{v_o}{R} \end{cases} \quad (23)$$

Based on the small-signal modeling method, the state variables x, duty ratios d, and the port voltages v are considered to have the dc values (X, D, V) and perturbations ($\hat{x}, \hat{d}, \hat{v}$):

$$\begin{cases} x = X + \hat{x} \\ d = D + \hat{d} \\ v = V + \hat{v} \end{cases} \quad (24)$$

Assume that the perturbations do not vary significantly over a switching cycle ($\hat{x} \ll X, \hat{d} \ll D, \hat{v} \ll V$) and the small-signal effect of Thevenin's voltage source can be negligible ($\hat{v}_{pv\_th} = 0$) [40]. One could substitute (24) into (15)-(18) and then average the four state equation sets regarding to their corresponding duty cycle. The last step is to neglect all of the second-order terms to obtain the small-signal model presented in matrix form:

$$\begin{cases} \dot{x} = Ax + Bu \\ y = Cx + Du \end{cases} \quad (25)$$

where x represents the state variable vector containing i_{L1}, i_{L2}, v_{C2}, and v_o, u represents the control variable vector containing d_1 and d_2, y represents the output variable vector. In this case,

the four state variables are also the system output. The small-signal model can be described as:

$$A = \begin{bmatrix} 0 & 0 & \frac{-n_2(1-D_1)}{L_1} & \frac{-(1-D_1)}{L_1} \\ 0 & 0 & \frac{n_2 D_2}{L_2} & \frac{-(1-D_2)}{L_2} \\ \frac{n_2(1-D_2)}{n_1 C_2} & \frac{D_2}{C_2} & \frac{1}{R_{pv\_th} C_2} & 0 \\ \frac{(1-D_1)}{n_1 C_o} & \frac{(1-D_2)}{n_2 C_o} & 0 & \frac{-1}{R C_o} \end{bmatrix}$$

$$x = \begin{bmatrix} \hat{i}_{L1} \\ \hat{i}_{L2} \\ \hat{v}_{C2} \\ \hat{v}_o \end{bmatrix} \quad B = \begin{bmatrix} \left(n_1 + \frac{(1+n_1)(1-D_2)}{(1-D_1)} \right) V_{C1} + V_o & 0 \\ 0 & \left(n_1 + \frac{(1+n_1)(1-D_2)}{(1-D_1)} \right) V_{C1} + V_o \\ \frac{-n_2 I_{L1}}{n_1 C_2} & \frac{I_{L2}}{C_2} \\ \frac{-I_{L1}}{n_1 C_o} & \frac{-I_{L2}}{n_2 C_o} \end{bmatrix}$$

$$u = \begin{bmatrix} \hat{d}_1 \\ \hat{d}_2 \end{bmatrix} \quad C = \begin{bmatrix} 1 & 0 & 0 & 0 \\ 0 & 1 & 0 & 0 \\ 0 & 0 & 1 & 0 \\ 0 & 0 & 0 & 1 \end{bmatrix} \quad D = \begin{bmatrix} 0 & 0 \\ 0 & 0 \\ 0 & 0 \\ 0 & 0 \end{bmatrix} \quad (26)$$

Using this model, the transfer functions for the PV port voltage and output port voltage to the duty cycle values of the main switches could be obtained based on the small-signal diagram shown in Fig. 8. For the system of proposed converter, the state variables are controlled by two control variables. The transfer function matrix can be represented as:

$$G = C(sI - A)^{-1} B + D$$

$$\frac{v_o}{d_1} = g_{11} = G(4,1) \quad \frac{v_{C2}}{d_1} = g_{21} = G(3,1)$$

$$\frac{v_o}{d_2} = g_{12} = G(4,2) \quad \frac{v_{C2}}{d_2} = g_{22} = G(3,2) \quad (27)$$

where $G(j,k)$ represents the transfer function of jth state variable to the kth control variable. These transfer functions can be calculated using the computer software such as MATLAB and are not presented because of their complexity. In order to design the closed-loop compensators separately, a decoupling network is introduced to decouple the interactive control loops [23]. In general derivation of decoupling network, the state variable vector can be written as $x = Gu^*$ where u^* is the modified input variable vector, $u^* = G^* u$. Therefore, $x = G G^* u$ and the goal here is to make $G G^*$ a diagonal matrix such that one output variable can be independently determined from one control input variable. According to $G^* = G^{-1} x u^{-1}$, G^* can be derived as:
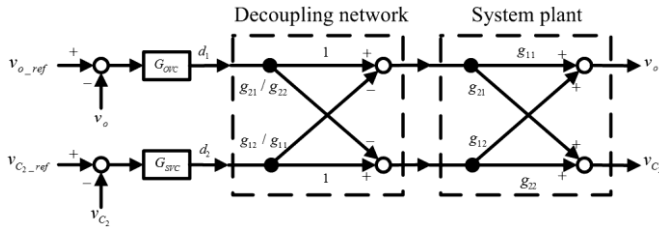
This article has been accepted for publication in a future issue of this journal, but has not been fully edited. Content may change prior to final publication.

TPEL-Reg-2012-10-1336   10

Fig. 8. Small-signal model with decoupling network and compensators in battery balance mode.

$$G^* = \begin{bmatrix} 1 & -\dfrac{g_{12}}{g_{11}} \\[3mm] -\dfrac{g_{21}}{g_{22}} & 1 \end{bmatrix} \tag{28}$$

Using (26)-(28), the system with cross-coupled control loops can be decoupled into system with two independent control loops. The control loops (OVC and SVC loops) can be designed from the following equations:

$$\frac{v_o(s)}{d_1(s)} = g_{11} - g_{12}\frac{g_{21}}{g_{22}}$$

$$\frac{v_{C2}(s)}{d_2(s)} = g_{22} - g_{12}\frac{g_{21}}{g_{11}} \tag{29}$$

B. Small-Signal Modeling in Battery Manage Mode

The small-signal model in battery manage mode can be derived by the same method. However, in this mode, the battery port voltage v_{C1} is considered as one of the state variables instead of the PV port voltage v_{C2}. The four state variables are now i_{L1}, i_{L2}, v_{C1}, and v_o while the control variables are still d_1 and d_2. The state-space averaged model in this mode could be represented as:

$$\begin{cases} L_1\dfrac{di_{L1}}{dt} = d_1 v_{C1} + (1-d_1)\dfrac{\dfrac{v_{C1}}{(1-d_1)} - n_2 v_{C2} - v_o}{n_1} \\[4mm] L_2\dfrac{di_{L2}}{dt} = d_2 v_{C2} + (1-d_2)\dfrac{-n_1 v_{C1} - v_o}{n_2} \\[4mm] C_1\dfrac{dv_{C1}}{dt} = i_{L1} + (2-d_1-d_2)\dfrac{n_1}{n_2}i_{L2} - \dfrac{v_{C1}}{R_b} \\[4mm] C_o\dfrac{dv_o}{dt} = (1-d_1)\dfrac{i_{L1}}{n_1} + (1-d_2)\dfrac{i_{L2}}{n_2} - \dfrac{v_o}{R} \end{cases} \tag{30}$$

Using (30), the small-signal model in this mode can be written as follows:

$$A = \begin{bmatrix} 0 & 0 & \dfrac{(1+n_1 D_1)}{L_1} & \dfrac{-(1-D_1)}{L_1} \\[3mm] 0 & 0 & \dfrac{-n_1(1-D_2)}{L_2} & \dfrac{-(1-D_2)}{L_2} \\[3mm] \dfrac{1}{C_1} & \dfrac{n_1(2-D_1-D_2)}{n_2 C_1} & \dfrac{-1}{R_b C_1} & 0 \\[3mm] \dfrac{(1-D_1)}{n_1 C_o} & \dfrac{(1-D_2)}{n_2 C_o} & 0 & \dfrac{-1}{RC_o} \end{bmatrix}$$

$$x = \begin{bmatrix} \hat{i}_{L1} \\ \hat{i}_{L2} \\ \hat{v}_{C1} \\ \hat{v}_o \end{bmatrix} \quad B = \begin{bmatrix} \left(\dfrac{n_1 n_2(1-D_1)}{(1+n_1)(1-D_2)} + n_2\right)V_{C2} + V_o & 0 \\[3mm] 0 & \left(\dfrac{n_1 n_2(1-D_1)}{(1+n_1)(1-D_2)} + n_2\right)V_{C2} + V_o \\[3mm] \dfrac{-n_1 I_{L2}}{n_2 C_1} & \dfrac{-n_1 I_{L2}}{n_2 C_1} \\[3mm] \dfrac{-I_{L1}}{n_1 C_o} & \dfrac{-I_{L2}}{n_2 C_o} \end{bmatrix}$$

$$u = \begin{bmatrix} \hat{d}_1 \\ \hat{d}_2 \end{bmatrix} \quad C = \begin{bmatrix} 1 & 0 & 0 & 0 \\ 0 & 1 & 0 & 0 \\ 0 & 0 & 1 & 0 \\ 0 & 0 & 0 & 1 \end{bmatrix} \quad D = \begin{bmatrix} 0 & 0 \\ 0 & 0 \\ 0 & 0 \\ 0 & 0 \end{bmatrix} \tag{31}$$

Similarly, the decoupling network can be used in this mode. The system control diagram with the decoupling network in battery manage mode is shown in Fig. 9. The transfer functions for the input and output voltage to duty cycle values can be extracted from the small-signal model. Therefore, the closed-loop controllers for OVC loop and BVC loop can be designed separately.

$$\frac{v_o}{d_1} = g_{11} = G(4,1) \quad \frac{v_{C1}}{d_1} = g_{21} = G(3,1)$$

$$\frac{v_o}{d_2} = g_{12} = G(4,2) \quad \frac{v_{C1}}{d_2} = g_{22} = G(3,2) \tag{32}$$

$$\frac{v_o(s)}{d_1(s)} = g_{11} - g_{12}\frac{g_{21}}{g_{22}}$$

$$\frac{v_{C1}(s)}{d_2(s)} = g_{22} - g_{12}\frac{g_{21}}{g_{11}} \tag{33}$$

Using equations (29) and (33), the system compensators could be designed with desired bandwidth, phase margin, and steady-state error. For the proposed converter, an integration unit should be incorporated to eliminate steady-state error of the system step responses. Although the steady-state error could be eliminated by adding an integral unit, the bandwidth would be reduced and may lead the system to be unstable.
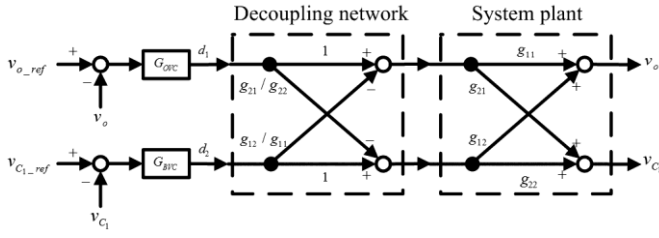
Fig. 9. Small-signal model with decoupling network and compensators in battery manage mode.

To achieve proper phase margin of $60^{\circ} \leq P.M. \leq 90^{\circ}$ and enough bandwidth, a lead unit should also be included in addition to the integral unit since the integral unit will lower the cutoff frequency and decrease the phase margin. The bandwidth of the BVC and SVC could be designed to be about one decade lower than OVC to achieve tight load regulation.

V. EXPERIMENTAL RESULTS

A 200-W laboratory prototype is built and tested under different solar irradiation or load demand as shown in Fig. 10. Furthermore, the transition of the operation modes and the control strategies are presented. The switches S_1-S_4 are implemented with one MOSFET IXFH88N30P ($R_{ds(on)}$= 0.04Ω, C_{oss}=950pF, TO-247,) S_5 is implemented with one MOSFET STW13NK100Z ($R_{ds(on)}$=0.56Ω, C_{oss}=455pF, TO-247.) Some other parameters used for the prototype is given in Table I. Again, all the control loops are implemented in a single microcontroller (TMS320F28335).

In Fig 11, the sun radiation is in period 1. For the first 40 seconds, there is very little sunlight so the MPPT is performed. However, once the level is too low or not available, MPPT is then disabled and the battery will become the only power source to supply the load. In Fig. 12(a) and 12(b), the sun irradiation is in period 2. The solar port is operated under MPPT and the battery port is discharged to supply part of the load. As the irradiation increases, the PV port will generate more power than the battery port. The increasing sun irradiation reaches period 3 in Fig. 13. The power generated from the PV port is now larger than the load demand so the battery port should be charged to store additional power. Although the batteries are charged but the charging voltage is not high enough to trigger the BVC loop. Thus, the solar panels still work under MPPT. As shown in Fig. 14, the maximum charging voltage for the batteries is reached in period 4. The BVC loop is then active to regulate the charging voltage and the MPPT is disabled.

At the beginning of Fig. 15, the load demand is set as 120W (R=1204Ω), the solar port is generating its maximum power and the deficit is provided by the battery port. At the time $t\approx32$ sec, load demand is decreased to 72W (R=2000Ω), which is lower than the power generated from the solar panels. The maximum solar power is still drawn from the panel after the load change and the batteries are charged by the additional solar power. It is observed that the current ripple of the battery is larger at the boundary of charging and discharging operations.
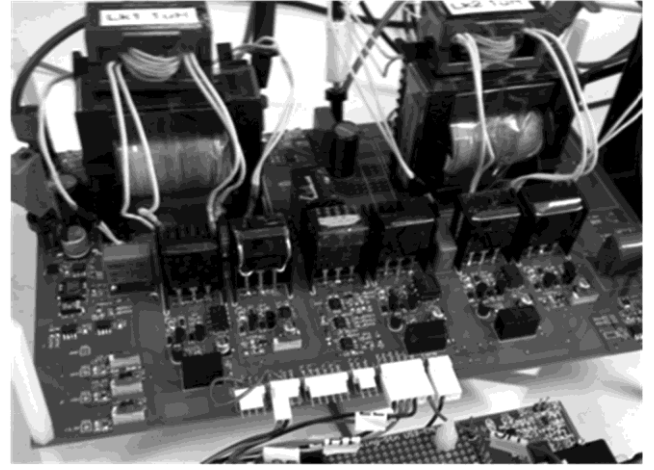

Fig. 10. Photograph of the three-port converter prototype.

TABLE I
CIRCUIT PARAMETERS

Parameter	Value
V_{bat}	48V
V_{pv_oc} (@800W/m^2)	52.8V
V_o	380V
P_{pv_max} (@800W/m^2)	200W
P_{o_max}	200W
f_{sw}	50kHz
n_1, n_2	4.44
L_1, L_2	52μH
L_{k1}, L_{k2}	1μH
C_{c1}, C_{c2}	470μF
C_o	47μF

When $t\approx58$ sec, the load is switched back to 120W so the batteries are discharged again..It can be observed that the solar port works under MPPT as long as the battery voltage is not too high. The transitions of the battery between charging and discharging are smooth and the operation mode does not need to be changed. It should be noted that even during the load change, MPPT is achieved and the output voltage is well regulated. This is one of the important features of three-port converters since MPPT and load regulation could not be maintained simultaneously for typical two-port converters [22].

Fig. 16(a) shows mode transition from SVC (mode 1: MPPT, R=900Ω) to BVC (mode 2: Battery voltage regulation, R=3600Ω) when the maximum charging voltage is reached. The PV port is operated under MPPT at the beginning to generate maximum solar power and the battery is discharged to share part of the load demand. It is noted that in mode 1, sometimes the solar power is slightly larger than the load demand therefore the batteries are temporally charged. The battery voltage in this case is clearly higher than discharging situation. However, the charging voltage during this short period is not high enough so the converter is still operated in mode 1. When a load change (from 80% to 20%) happened at $t\approx50$ sec, the battery is suddenly charged with a large current and the battery voltage is then increased dramatically. When the charging voltage is higher than the maximum setting, the operation mode is switched to mode 2 immediately to regulate the battery voltage and prevent overcharging.
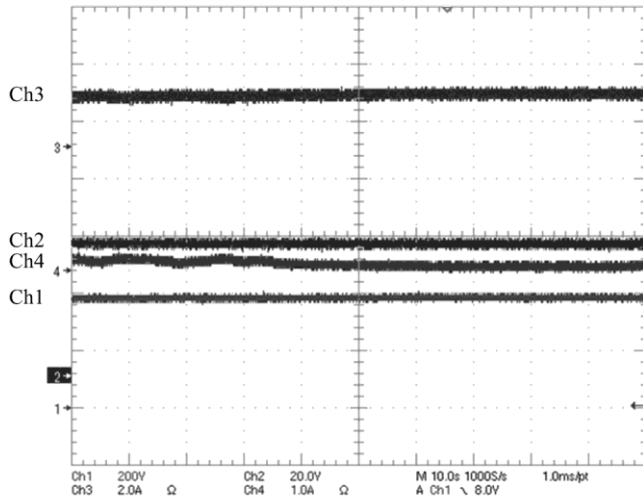
This article has been accepted for publication in a future issue of this journal, but has not been fully edited. Content may change prior to final publication.

TPEL-Reg-2012-10-1336   12

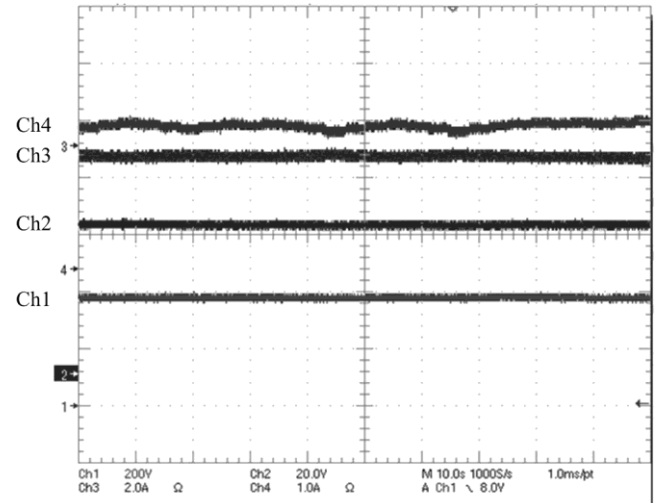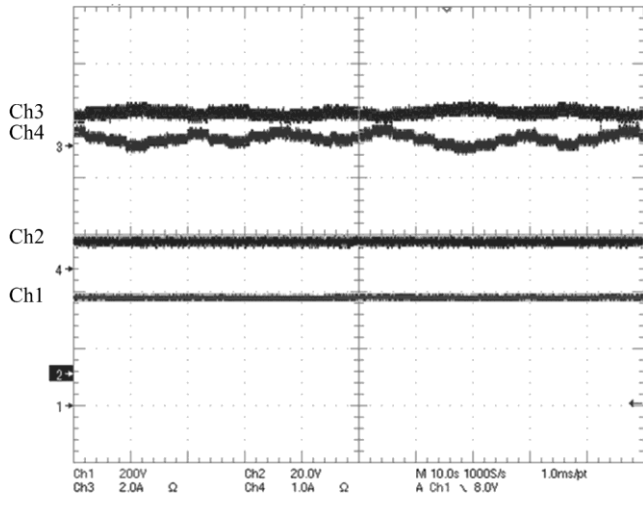Fig. 11. Measured waveforms of mode operation in period 1. (R=3030Ω, Ch1:V_o, Ch2: V_b, Ch3: I_b, Ch4: I_{pv}).

Fig. 13. Measured waveforms of mode operation in period 3. (R=3030Ω, Ch1:V_o, Ch2: V_b, Ch3: I_b, Ch4: I_{pv}).
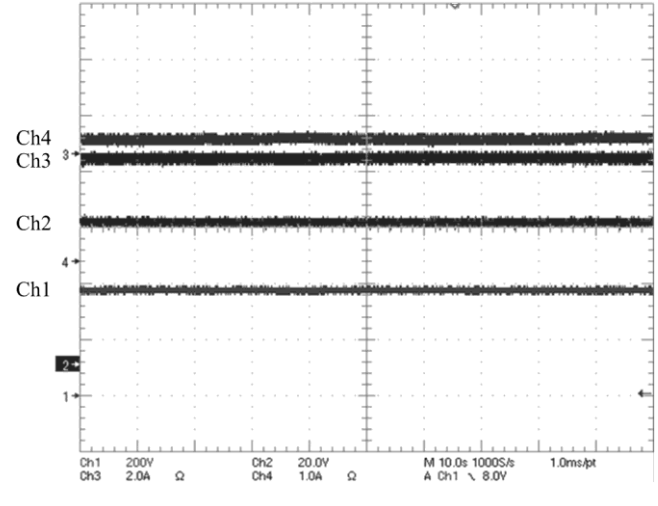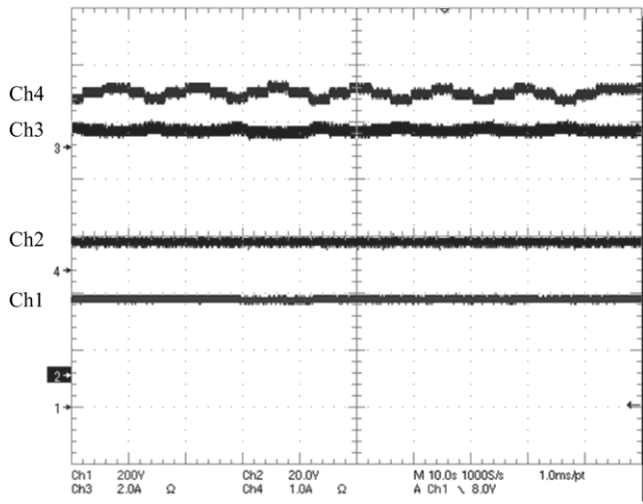

(a)

Fig. 14. Measured waveforms of mode operation in period 4. (R=3030Ω, Ch1:V_o, Ch2: V_b, Ch3: I_b, Ch4: I_{pv}).

(b)

Fig. 12. Measured waveforms of mode operation in period 2. (a) Lower solar irradiation level. (b) Higher solar irradiation level. (R=1204Ω, Ch1:V_o, Ch2: V_b, Ch3: I_b, Ch4: I_{pv}).
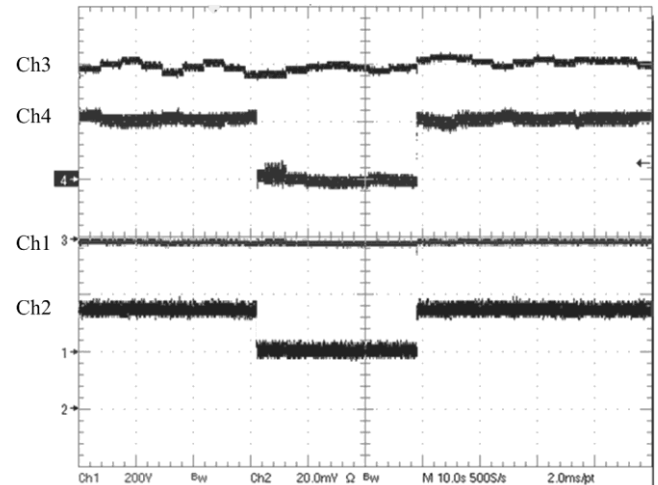

Fig. 15. Measured waveforms of load step response under SVC. (Ch1:V_o, Ch2: V_b, Ch3: I_{pv}, Ch4: I_b).

This article has been accepted for publication in a future issue of this journal, but has not been fully edited. Content may change prior to final publication.

TPEL-Reg-2012-10-1336   13

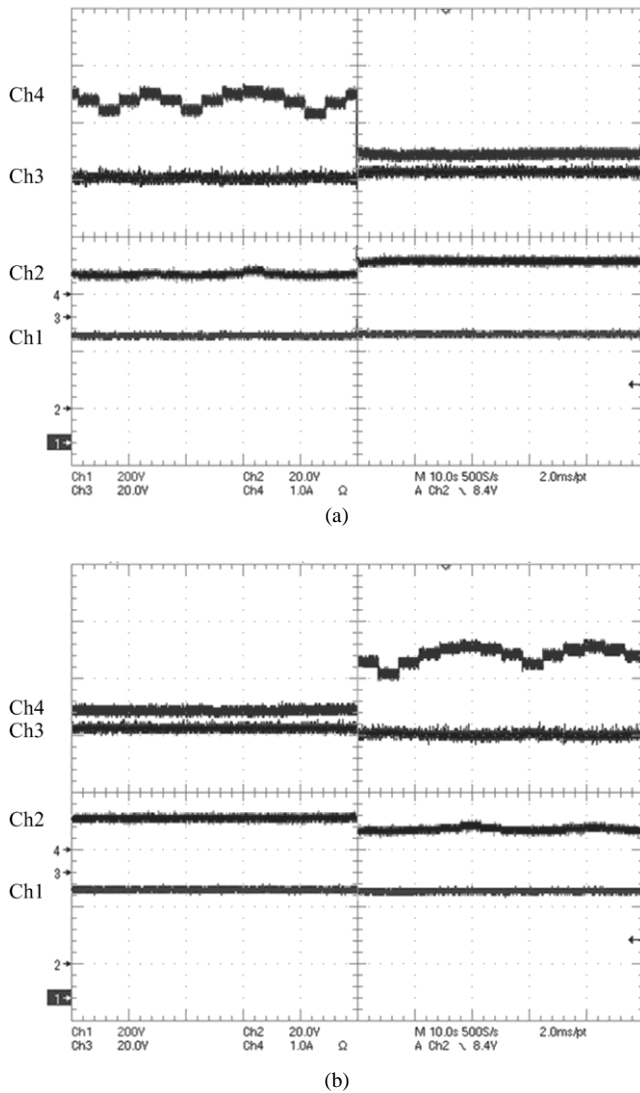Fig. 16. Autonomous mode transition. (a) Mode 1 to mode 2. (b) Mode 2 to mode 1. (Ch1:V_o, Ch2: V_b, Ch3: I_b, Ch4: I_{pv}).

It can be seen that in mode 2, the solar panel is no longer operated around the maximum power point but the right side of it. Fig. 16(b) shows the transition from mode 2 to mode 1 when the load is suddenly increased. The SVC will take over the control on the PV port since the maximum setting of the battery voltage could not be met. Similarly, sometimes the batteries could be slightly charged according to the intensity of solar irradiation. Again, no matter what mode is operated for the PV port, the output voltage will be always regulated at 380V.

VI. CONCLUSION AND FUTURE WORK

A high step-up three-port DC-DC converter for stand-alone power systems is proposed to integrate solar and battery power. In the proposed topology, two coupled inductors are employed as voltage gain extension cells for high voltage output applications. Two sets of buck-boost type active clamp circuits are used to recycle the energy stored in the leakage inductors and improve the efficiency. The proposed switching strategy

only needs to control two duty ratios in different operation modes. The experimental results validate the functionality of the proposed converter under different solar irradiation level and load demand. The charging/discharging operation of battery could be achieved without changing the operation mode therefore MPPT operation will not be interrupted. In light load condition, once the charging voltage is higher than the preset level, the operation mode will be changed rapidly to protect the battery from overcharging. The highest converter efficiency is measured as 90.1% at 110W. The control method of battery port could be modified for the grid-connected applications. Discussion from control viewpoints including moving the effect of RHP-zeros to particular output, limitations on sensitivity of the system, trade-offs in the feedback controller design and implementation of improved decoupling method should be presented in our future work.

REFERENCES

[1] S. H. Choung, and A, Kwasinski, "Multiple-input DC-DC converter topologies comparison," in *Proc. IECON*, 2008, pp. 2359-2364.
[2] A. Huang, "FREEDM system – a vision for the future grid," in *Proc. IEEE Power and Energy Soc. (PES) Gen. Meeting*, 2010, pp. 1-4.
[3] W. Li and X. He, "Review of nonisolated high-step-up DC/DC converters in photovoltaic grid-connected applications," *IEEE Trans. Ind. Electron.*, vol. 58, no. 4, pp. 1239-1250, Apr. 2011.
[4] T.-F. Wu, Y.-S. Lai, J.-C. Hung, and Y.-M. Chen , "Boost Converter With Coupled Inductors and Buck–Boost Type of Active Clamp," *IEEE Trans. Ind. Electron.*, vol.55, no.1, pp.154-162, Jan. 2008.
[5] W. G. Imes and F. D. Rodriguez, "A two-input tri-state converter for spacecraft power conditioning," in *Proc. AIAA Int. Energy Convers. Eng. Conf.*, 1994, pp. 163–168.
[6] F. D. Rodriguez and W. G. Imes, "Analysis and modeling of a twoinput DC/DC converter with two controlled variables and four switched networks," in *Proc. AIAA Int. Energy Conf.*, 1994, pp. 163-168.
[7] B. G. Dobbs and P. L. Chapman, "A multiple-input DC–DC converter topology," *IEEE Power Electron. Lett.*, vol. 1, no. 1, pp. 6–9, Mar. 2003.
[8] R. J. Wai, Ch. Y. Lin, J. J. Liaw, and Y. R. Chang, "Newly designed ZVS multi-input converter," *IEEE Trans. Ind. Electron.*, vol. 58, no. 2, pp. 555-566, Feb. 2011.
[9] L. Solero, A. Lidozzi and J. A. Pomilio,. "Design of multiple-input power converter for hybrid vehicles," in Proc. IEEE Appl. Power Electron. Conf., 2004, pp. 1145-1151.
[10] F. Nejabatkhah, S. Danyali, S. H. Hosseini, M. Sabahi and S. M. Niapour, "Modeling and control of a new three-input DC-DC boost converter for hybrid PV/FC/battery power system," IEEE Trans. Power Electron., vol. 23, no. 2, pp. 782-792, Mar. 2008.
[11] J. Jung and A. Kwasinski, "A multiple-input SEPIC with a bi-directional input for modular distributed generation and energy storage integration," in *Proc. IEEE Appl. Power Electron. Conf.*, 2011, pp. 28-34.
[12] G.-J. Su and F. Z. Peng, "A low cost, triple-voltage bus DC–DC converter for automotive applications," in *Proc. IEEE Appl. Power Electron. Conf.*, 2005, pp. 1015–1021.
[13] A. Kwasinski, "Identification of feasible topologies for multiple-input DC-DC converters," *IEEE Trans. Power Electron.*, vol. 24, pp. 856–861, Mar. 2009.
[14] S. Yu and A. Kwasinski, "Analysis of a soft-switching technique for isolated time-sharing multiple-input converters," in *Proc. IEEE Appl. Power Electron. Conf.*, 2012, pp. 844-851.
[15] D. Liu and H. Li, "A ZVS bi-directional DC–DC converter for multiple energy storage elements," *IEEE Trans. Power Electron.*, vol. 21, no. 5, pp. 1513-1517, Sep. 2006.
[16] H. Tao, A. Kotsopoulos, J. L. Duarte, and M. A. M. Hendrix, "Triple-half-bridge bidirectional converter controlled by phase shift and PWM," in *Proc. IEEE Appl. Power Electron. Conf.*, Mar. 2006, pp. 1256–1262.
[17] L. Wang, Z. Wang, and H. Li, "Asymmetrical duty cycle control and decoupled power flow design of a three-port bidirectional DC-DC converter for fuel cell vehicle application," *IEEE Trans. Power Electron.*, vol. 27, no. 2, pp. 891-903, Feb. 2012.

This article has been accepted for publication in a future issue of this journal, but has not been fully edited. Content may change prior to final publication.

TPEL-Reg-2012-10-1336   14

[18] Y.-M. Chen, Y.-C. Liu, and F.-Y. Wu, "Multi-input DC/DC converter based on the multiwinding transformer for renewable energy applications," *IEEE Trans. Ind. Appl.*, vol. 38, no. 4, pp. 1096-1104, Jul./Aug. 2002.

[19] H. Tao, A. Kotsopoulos, J. L. Duarte, and M. A. M. Hendrix, "Transformercoupled multiport ZVS bidirectional DC–DC converter with wide input range," *IEEE Trans. Power Electron.*, vol. 23, no. 2, pp. 771–781, Mar. 2008.

[20] C. Zhao, S. D. Round, and J. W. Kolar, "An isolated three-port bidirectional DC–DC converter with decoupled power flow management," *IEEE Trans. Power Electron.*, vol. 23, no. 5, pp. 2443–2453, Sep. 2008.

[21] H. Krishnaswami, and N. Mohan "Three-port series resonant DC-DC converter to interface renewable energy sources with bidirectional load and energy storage ports," *IEEE Trans. Power Electron.*, vol. 24, no. 10, pp. 2289-2297, Oct. 2009.

[22] H. Al-Atrash, F. Tian, and I. Batarseh, "Tri-modal half-bridge converter topology for three-port interface," *IEEE Trans. Power Electron.*, vol.22, no. 1, pp. 341–345, Jan. 2007.

[23] Z. Qian, O. Abdel-Rahman, H. Al-Atrash, and I. Batarseh, "Modeling and control of three-port dc/dc converter interface for satellite applications," *IEEE Trans. Power Electron.*, vol. 25, no. 3, pp. 637-649, Mar. 2010.

[24] H.Wu, K. Sun, R. Chen, H. Hu, and Y. Xing, "Full-bridge three-port converters with wide input voltage range for renewable power systems," *IEEE Trans. Power Electron.*, vol. 27, no. 9, pp. 3965-3974, Sep. 2012.

[25] N. D. Benavides and P. L. Chapman, "Power budgeting of a multipleinput buck-boost converter," *IEEE Trans. Power Electron.*, vol. 20, no.6, pp. 1303–1309, Nov. 2005.

[26] T. Suntio, J. Leppäaho, J. Huusari and L. Nousiainen, "Issues on solar-generator interfacing with current-fed MPP-tracking converters," *IEEE Trans. Power Electron.*, vol. 25, no. 9, pp. 2409-2419, Sep. 2010.

[27] H. Al-Atrash, I. Batarseh, and K. Rustom, "Statistical modeling of DSP based hill-climbing MPPT algorithms in noisy environments," in *Proc IEEE Appl. Power Electron. Conf.*, 2005, pp. 1773-1777.

[28] R. W. Erickson and D. Maksimovic, *Fundamentals of Power Electronics*, 2nd ed. New York: Springer, 2001.

[29] L. Nousiainen, J. Puukko, A. Mäki, T. Messo, J. Huusari, J. Jokipii, J. Viinamäki, D. T. Lobera, S. Valkealahti, and T. Suntio, "Photovoltaic Generator as an Input Source for Power Electronic Converters" *IEEE Trans. Power Electron.* (Early Access)

[30] T. Suntio, J. Huusari, and J. Leppäaho, "Issues on solar-generator interfacing with voltage-fed mpp-tracking converters," *EPE Journal*, vol. 20, no. 3, pp. 40-47, Sept. 2010.

[31] T. Suntio, J. Leppäaho, J. Huusari, and L. Nousiainen, "Issues on solar-generator interfacing with current-fed mpp-tracking converters," *IEEE Trans. Power Electron.*, vol. 25, no. 9, pp. 2409-2419, Sept. 2010.

[32] J. Puukko, T. Messo, and T. Suntio, "Effect of photovoltaic generator on a typical vsi-based three-phase grid-connected photovoltaic inverter dynamics," in *IET Renewable Power Generation Conf.*, Edinburgh, U.K., Sept. 2011, pp. 1-6.

[33] J. Gow and C. Manning, "Development of a photovoltaic array model for use in power electronics simulation studies," *IEE Proc. Electric Power Applications*, vol. 146(6), pp. 193-200, 2002.

[34] Ray-Lee Lin, and Yi-Fan Chen, "Equivalent circuit model of light-emitting-diode for system analyses of lighting drivers," *Industry Applications Society Annual Meeting 2009*, pp. 1-5.

[35] A. Chatterjee, and A. Keyhani, "Thevenin's equivalent of photovoltaic source models for MPPT and power grid studies," *IEEE Power and Energy Society General Meeting*, pp.1-7, July 2011.

[36] Z. Batushansky, and A. Kuperman, "Thevenin-based approach to PV arrays maximum power prediction," in *Proc. IEEE 26th Convention of Electrical and Electronics Engineers in Israel*, pp. 598-602, Nov. 2010.

[37] S. Chowdhury, G. A. Taylor, S. P. Chowdhury, A. K. Saha, and Y. H. Song, "Modelling, simulation and performance analysis of a PV array in an embedded environment," in *Proc. Univ. Power Eng. Conf.*, 2007, pp. 781-785.

[38] H. Patangia, S. G. Gourisetti, A. Siddiqui, and S. Sharma, "A simplified PV model for low power MPPT controller design," in *Proc. IEEE Asia-Pacific Conf. Circuits Syst.*, pp. 680-683, 2010.

[39] M. G. Villalva, J. R. Gazoli, and E. R. Filho, "Comprehensive approach to modeling and Simulation of Photovoltaic Arrays," *IEEE Trans. Power Electron.*, vol. 24, no. 5, pp. 1198-1208, May 2009.

[40] C. Hutchens, W. Yu; J.-S. Lai, "Modeling and control of charge-pumped reboost converter for PV applications," in *Proc. IEEE Control and Modeling for Power Electron.*, 2010, pp. 1-5.

Yen-Mo Chen (S'12) received the B.S. degree in electrical engineering from Chung Yuan Christian University, Jungli, Taiwan in 2004 and the M.S. degree in electrical engineering from National Central University, Jungli, Taiwan in 2006. He is currently working toward his Ph.D. degree in the FREEDM System Center, Department of Electrical and Computer Engineering at North Carolina State University, Raleigh. His research interests are hybrid renewable energy systems, power converter design, smart grids power management and control systems.

Alex Q. Huang (S'91–M'94–SM'96–F'05) received the B.S. degree from Zhejiang University, Hangzhou, China, in 1983 and the M.S. degree from Chengdu Institute of Radio Engineering, Chengdu, China, in 1986, both in electrical engineering, and the Ph.D. degree in electrical engineering from Cambridge University, Cambridge, U.K., in 1992.

From 1992 to 1994, he was a Research Fellow at Magdalene College, Cambridge. From 1994 to 2004, he was a Professor at the Bradley Department of Electrical and Computer Engineering, Virginia Polytechnic Institute and State University, Blacksburg. Since 2004, he has been with North Carolina State University, Raleigh, and is currently the Progress Energy Distinguished Professor of Electrical and Computer Engineering and directs the NSF FREEDM Systems ERC, NCSU Advanced Transportation Energy Center (ATEC), and NCSU Semiconductor Power Electronics Center (SPEC). Since 1983, he has been involved in the development of modern power semiconductor devices and power integrated circuits. He fabricated the first IGBT power device in China in 1985. He is the inventor and key developer of the emitter turnoff thyristor technology. His current research interests are utility power electronics, power management microsystems, and power semiconductor devices. He has published more than 200 papers in the international conferences and journals, and has 14 U.S. patents.

Dr. Huang is the recipient of the National Science Foundation (NSF) CAREER award and the prestigious R&D 100 Award.

Xunwei Yu (S'07) received the M.S. degree in electrical engineering from Huazhong University of Science and Technology, Wuhan, China, in 2007. He is currently working toward his Ph.D. degree in the FREEDM System Center, Department of Electrical and Computer Engineering at North Carolina State University, Raleigh. His research interests are in design of power conversion, digital control technique, integration of distributed renewable energy resources, and microgrids system power management.